Assessment of deviatoric lattice strain uncertainty for polychromatic X-ray microdiffraction experiments

Andrew Poshadel,[a]* Paul Dawson[a] and George Johnson[b]

[a]Sibley School of Mechanical and Aerospace Engineering, 196 Rhodes Hall, Cornell University, Ithaca, NY 14853, USA, and [b]University of California, 6149 Etcheverry Hall, Berkeley, CA 94720, USA. E-mail: acp42@cornell.edu

X-ray microdiffraction is a powerful technique for conducting high-spatial-resolution lattice strain measurements. However, there has been limited validation of the technique to date. An experiment was conducted at the Advanced Light Source to assess the uncertainty of deviatoric lattice strains measured using polychromatic X-ray microdiffraction. It is shown that the measurement uncertainty is different for each component of the deviatoric lattice strain tensor. Monte Carlo simulations of the experiment are used to explain the differences in uncertainty. The simulations point to the existence of spurious deformation modes that arise erroneously in the strain calculation owing to measurement noise and limited pole figure coverage. Methods for reducing measurement uncertainty are proposed.

Keywords: polychromatic; X-ray; microdiffraction; lattice strain; uncertainty; *in situ*.

1. Introduction

X-ray microdiffraction is a high-spatial-resolution tool for measuring crystallographic orientation and strain in crystalline materials (Chung & Ice, 1999; Ice & Pang, 2009). High spatial resolution is achieved using an X-ray beam with cross-sectional dimension of the order of 1 µm. A two-dimensional spatial map of the orientation and strain fields can be obtained by translating the sample through the beam (Tamura *et al.*, 2003, 2005). An extension of this technique enables three-dimensional spatial resolution (Larson *et al.*, 2002). When the grain size is larger than the beam cross section, orientation and strain are measured with subgrain spatial resolution.

The full strain tensor $\boldsymbol{\varepsilon}$ can be additively decomposed into volumetric and deviatoric components,

$$\boldsymbol{\varepsilon} = \varepsilon_{\mathrm{vol}} \boldsymbol{I} + \boldsymbol{\varepsilon}', \tag{1}$$

where $\varepsilon_{\mathrm{vol}} = \mathrm{tr}(\boldsymbol{\varepsilon})/3$ is the volumetric strain, $\boldsymbol{\varepsilon}'$ is the deviatoric strain, and $\boldsymbol{I}$ is the second-order identity tensor (Reddy, 2008). The volumetric strain is due purely to dilatation. Deviatoric strain, in contrast, is due to distortional shape change of the crystal lattice, independent of dilatation.

Microdiffraction experiments can be conducted using either polychromatic or monochromatic X-rays (Chung & Ice, 1999; Ice & Pang, 2009). The Laue pattern captured in a single polychromatic image can be used to calculate the deviatoric lattice strain tensor. Monochromatic energy scans consist of multiple monochromatic images taken over a range of energies. An energy scan can be used to calculate the projection of

the lattice strain tensor in the scattering vector direction. Energy scans of a minimum of four scattering vectors are required to determine the full lattice strain tensor. Alternately, a polychromatic image can be coupled with one or more energy scans to determine the full lattice strain tensor. The coupling of polychromatic and monochromatic experiments to determine the full lattice strain tensor offers a significant reduction to the data collection time required for the multiple energy scan method. In this investigation we focus on deviatoric lattice strain measurement using polychromatic X-rays.

While polychromatic X-ray microdiffraction possesses much potential, there has been limited validation of its ability to resolve the entire deviatoric lattice strain tensor. A proof-of-concept experiment on a bent silicon wafer (Larson *et al.*, 2002) demonstrated the technique's capability to measure normal strain components. However, shear strain components were not reported. Validation studies have also been performed on unstrained crystals used for calibration of the strain measurements (Chung & Ice, 1999). Uncertainty analysis by Zhang (2009) dealt only with normal strain components and employed a simplified geometric model.

In this investigation the component-by-component uncertainty of deviatoric lattice strain measured using polychromatic X-ray microdiffraction was assessed. Experiments were performed at the Advanced Light Source on a thin wire specimen loaded *in situ* under uniaxial tension. Monte Carlo simulations of the experiment were used to quantify the uncertainty in the measured strain components. The simulations point to the existence of spurious deformation modes

237

that arise erroneously in the strain calculation owing to measurement noise and limited pole figure coverage. These spurious deformation modes affect specific components of the deviatoric lattice strain tensor. As a result, measurement uncertainties are different for each strain component.

2. Methodology

2.1. Diffraction experiment

An experiment was conducted at beamline 12.3.2 of the Advanced Light Source (Kunz *et al.*, 2009) to assess the error in deviatoric lattice strain measurements conducted using polychromatic X-ray microdiffraction. An AISI 304 stainless steel wire was loaded *in situ* under uniaxial tension using a custom-built load frame (Fig. 1). The wire was wound around the two load frame capstans. Load was applied by pulsing a geared stepper motor, which turned the drive capstan, tightening the wire. The reaction capstan was attached to a linear slider bearing and rested on two load cells, which measured the axial force on the wire. The wire was loaded incrementally in a series of six load steps in the elastic regime. At each load step an area scan was performed in which 100 diffraction images were taken in a 10 μm × 10 μm grid near the center of a large grain.

The experimental geometry is presented in Fig. 2. The wire axis is inclined at a 45° angle to the incoming beam. The incoming 1 μm × 1 μm polychromatic X-ray beam impinges on a subgrain region of the wire specimen. It also impinges on grains of LaB_6 powder, applied to the surface of the wire for calibration purposes. Diffracted X-rays are produced for each grain and set of crystal lattice planes that satisfy Bragg's law. A subset of the diffracted X-rays is sampled by a circular MARCCD area detector positioned 79.5 mm above the sample volume. Detector spatial distortion is corrected by the MAR acquisition software. The detector diameter is 133 mm, and the padded detector image size is 1024 pixels × 1024 pixels. The right-handed Cartesian laboratory coordinate
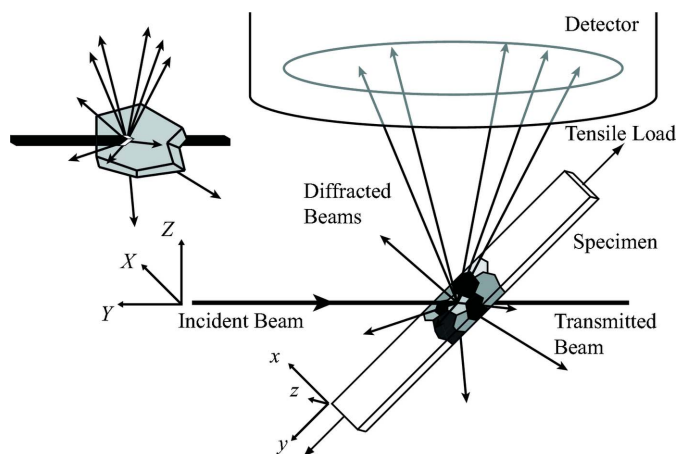

Figure 2
Schematic of the diffraction experiment showing the laboratory and sample coordinate systems.

system XYZ is defined such that the Y-direction is antiparallel to the direction of the incoming beam. The right-handed Cartesian sample coordinate system xyz is defined with the y-direction parallel to the wire axis. For a perfectly aligned apparatus, the laboratory X-direction is parallel to the sample x-direction, and the two coordinate systems are related by a rotation of 45° about the common X- and x-direction.

Prior to the experiment, the wire was rolled to obtain a rectangular 186 μm × 107 μm cross section. It was then annealed in a vacuum-tube furnace. After 30 min at 1353 K the furnace was turned off and allowed to air cool, while still maintaining a vacuum inside the tube. The annealing process alleviated residual elastic strain and produced large grain size. The largest grains extended almost entirely across the width of the wire, producing a quasi-bamboo microstructure (Fig. 3).

Local stress states within polycrystals are, in general, different from the macroscopic stress. However, because of the quasi-bamboo microstructure, the local stress states near the centers of large grains can be approximated as homogenous and equal to the macroscopic stress. The macroscopic stress is computed from the axial load and cross-sectional area of the wire. Hooke's law is then used to calculate lattice strain from the stress, crystallographic orientation and anisotropic crystal stiffness. The orientation of the crystal interrogated in the experiment, expressed as a Rodrigues vector, is {−0.1810; −0.2245; 0.2514}. The Rodrigues vector is an angle-axis parameterization of the rotation that maps the crystal-
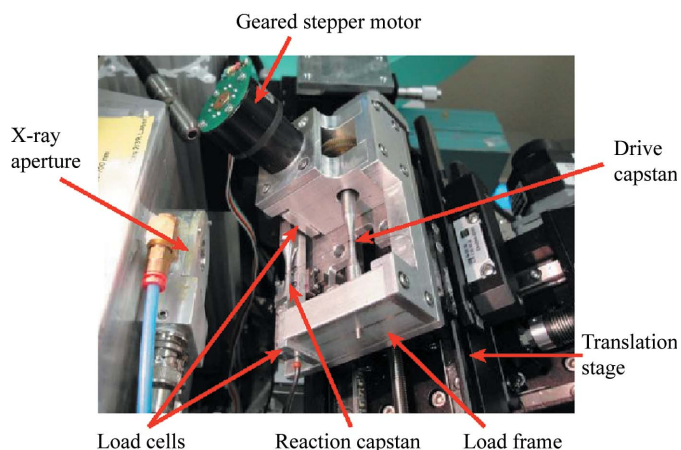

Figure 1
The custom-built load frame used to load the wire specimen *in situ*. The wire specimen is wound around the two capstans. The wire is barely visible in this photograph owing to its small cross section (186 μm × 107 μm). The distance between the capstans is 34 mm.
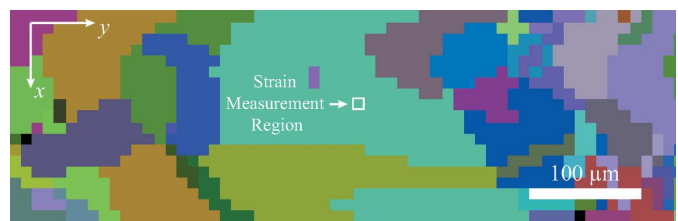

Figure 3
Orientation map depicting the section of the stainless steel wire specimen that encompasses the strain measurement region. The entire width of the wire in the x-direction is captured in the image.

lographic axes to the sample axes (Frank, 1988). Single-crystal elastic constants were obtained from Ledbetter (2001). The theoretical deviatoric lattice strains, computed by using Hooke's law and subtracting the volumetric strain, were compared with the measured deviatoric lattice strains.

2.2. Deviatoric lattice strain calculation

A representative diffraction image is presented in Fig. 4. Diffraction peaks are high-intensity regions that correspond to the locations where diffracted X-rays intersect the detector. The spatial intensity field corresponding to each diffraction peak is fit using a two-dimensional Lorentzian function. Peak fitting is performed using *X-ray Microdiffraction Analysis Software* (*XMAS*) (Chung & Ice, 1999). The centers of the fitted diffraction peaks are taken to be the peak positions on the detector. The directions of the diffracted beams are calculated from peak positions and the experimental geometry. Scattering vector directions are calculated using Bragg's law, which states that scattering vectors bisect the incoming and diffracted beams. Scattering vectors are aligned with the lattice plane normals. Thus, the scattering vector direction is equivalent to the lattice plane unit normal. The set of unit normals for each diffraction image is indexed using *XMAS* to identify the grain and crystallographic plane corresponding to each normal. The indexing process also identifies the crystallographic orientations of the diffracting grains.

A geometric model is employed in the lattice plane unit normal calculation. The model describes the position (XYZ), pitch (X-rotation) and yaw (Z-rotation) of the detector relative to the sample position and incoming beam direction. Model parameters are determined from LaB_6 calibrant data. For each calibrant pattern an iteration is performed on the geometric model parameters and crystal orientation. The iteration seeks to minimize the angles between theoretical and measured diffracted beams. The LaB_6 powder is assumed to be unstrained. Geometric model parameters are averaged for each load step. The parameters are different for each load step
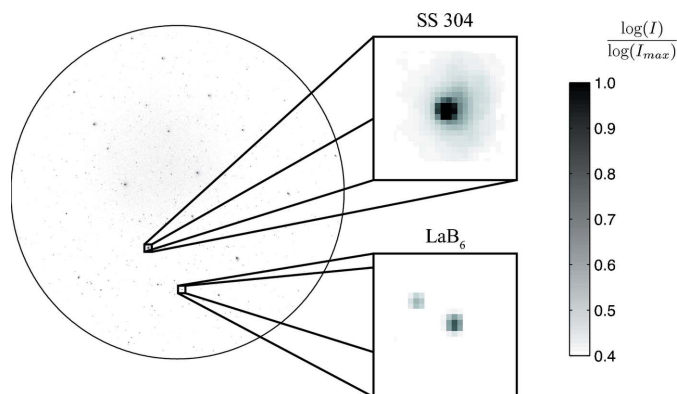
owing to sample movement during loading and repositioning of the detector between load steps.

Deviatoric lattice strain is calculated from the stainless steel lattice plane unit normals. The customary approach to strain calculation involves reconstructing the reciprocal lattice (Chung & Ice, 1999). We, however, adopt a mechanics-based approach similar to Edmiston *et al.* (2011) for polychromatic experiments. The two methods describe the same physics and produce similar results. However, the mechanics-based approach offers additional insight into the deformation kinematics.

The mechanics-based method utilizes the deformation gradient tensor (Reddy, 2008). The deformation gradient $\boldsymbol{F}$ maps differential material fibers (or vectors) from a reference configuration $\mathcal{B}_0$ to a deformed configuration $\mathcal{B}$. For crystalline materials the deformation gradient may be defined locally at points within a grain to aid in the interpretation of diffraction data.

Following the notation of Marin & Dawson (1998), the local deformation can be multiplicatively decomposed into a lattice-uncoupled plastic deformation $\boldsymbol{F}^p$, followed by a lattice-coupled deformation $\boldsymbol{F}^*$,

$$\boldsymbol{F} = \boldsymbol{F}^*\boldsymbol{F}^p. \qquad (2)$$

This decomposition introduces an intermediate configuration $\bar{\mathcal{B}}$. The decomposition is illustrated schematically in Fig. 5. The lattice-uncoupled plastic deformation is produced by processes such as homogeneous crystallographic slip and diffusion. The lattice structure and orientation are unaltered by lattice-uncoupled plastic deformation, and so lattice vectors are unchanged by the deformation. The lattice response is therefore uncoupled from changes in material fibers induced by this part of the total deformation. The lattice-coupled deformation includes lattice rotation, elastic stretch and certain types of inelastic processes, such as twinning. In contrast to the lattice-uncoupled behavior, for lattice-coupled deformation modes the lattice vectors transform in the same manner as material fibers. Thus, the lattice response is directly coupled to changes in the material fibers associated with the deformation. Lattice-uncoupled deformation does not affect diffraction peak positions because lattice structure
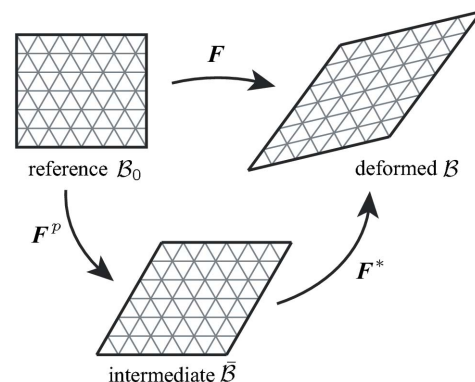

Figure 4
Representative diffraction image. Intensity is plotted on a logarithmic scale. High-intensity spots are from the stainless steel specimen. Low-intensity spots are primarily from the LaB_6 calibrant.

Figure 5
The local deformation $\boldsymbol{F}$ is decomposed into a lattice-uncoupled plastic deformation $\boldsymbol{F}^p$, followed by a lattice-coupled deformation $\boldsymbol{F}^*$.

research papers

and orientation are unaltered. Changes in diffraction peak positions are produced only by the lattice-coupled deformation.

The lattice-coupled part of the deformation gradient tensor F^* is recovered and used to calculate deviatoric lattice strain and rotation. The lattice strain and rotation calculation is essentially a geometric mapping problem that consists of finding F^* which best maps between two sets of lattice plane unit normals, subject to an imposed volumetric constraint. Lattice plane normals transform according to

$$F^{*T} \hat{\mathbf{n}}^i = c^i \hat{\mathbf{n}}_0^i, \tag{3}$$

where $\hat{\mathbf{n}}^i$ is a lattice plane unit normal in the deformed configuration, $\hat{\mathbf{n}}_0^i$ is the corresponding lattice plane unit normal in the reference configuration, and c^i is a scale factor. Superscript $i = 1, 2, \ldots, m$ indexes the plane unit normals associated with the m diffraction peaks. The derivation of (3) can be found in Appendix A. Since polychromatic diffraction does not provide information about volumetric deformation, a volumetric constraint must be specified. This is accomplished by setting one of the scale factors equal to unity,

$$c^m = 1. \tag{4}$$

The lattice plane unit normal mapping (3) represents a system of equations. Lattice plane unit normals in the unstrained reference configuration are either measured experimentally prior to deformation or calculated from the undeformed crystal geometry. Unit normals in the deformed configuration are measured by the diffraction experiment. Each diffraction peak contributes a vector equation with three components, for a total of $3m$ scalar equations. There are nine unknown components of the deformation gradient and $m - 1$ unknown scale factors, following the imposition of the volumetric constraint, resulting in a total of $m + 8$ unknowns. Therefore m must be greater than or equal to 4 to solve the system of equations uniquely. Additionally, there must exist a subset of four plane normals such that any three normals chosen from the subset are linearly independent (Chung & Ice, 1999). A least-squares optimization is established to solve for the components of the deformation gradient and unknown scale factors. Linearity enables the optimization to be written as a matrix inversion, resulting in fast computation.

Once calculated, F^* is multiplicatively decomposed into stretch and rotation components using polar decomposition

$$F^* = V^* R^*, \tag{5}$$

where V^* is the left stretch tensor and R^* is the lattice rotation matrix. The stretch tensor is further decomposed

into a volumetric scaling $J^* = \det F^*$ and an isochoric stretch $\tilde{V}^*$,

$$V^* = J^{*1/3} \tilde{V}^*. \tag{6}$$

This decomposition separates the isochoric stretch from the arbitrary volumetric scaling imposed by the volumetric constraint (4). Principal values and directions of the isochoric stretch tensor are computed using eigenvalue analysis. Principal deviatoric lattice strains are calculated from the natural logarithms of the principal values of $\tilde{V}^*$. A change of basis relates the components of the deviatoric lattice strain tensor in the principal and sample bases (Reddy, 2008).

The lattice rotation matrix can be decomposed into a series of three rotations. For analysis, we employ the decomposition

$$R^* = R_z^* R_y^* R_x^*, \tag{7}$$

where R_x^*, R_y^* and R_z^* represent rotations about the sample coordinate axes. The angular rotations about the sample x, y and z axes are represented by α, β and γ, respectively.

3. Deviatoric lattice strain measurements

Deviatoric lattice strain measurements are presented in Fig. 6. Each data point corresponds to 100 measurements taken in a 10 µm × 10 µm area scan. Since the measurements were taken near the center of a large grain, the strain field is approximately homogeneous over the sampled region. The average strain measurement for each area scan is plotted with a marker. Error bars represent the full range of measured strain. Theoretical strain, calculated using anisotropic elasticity, is
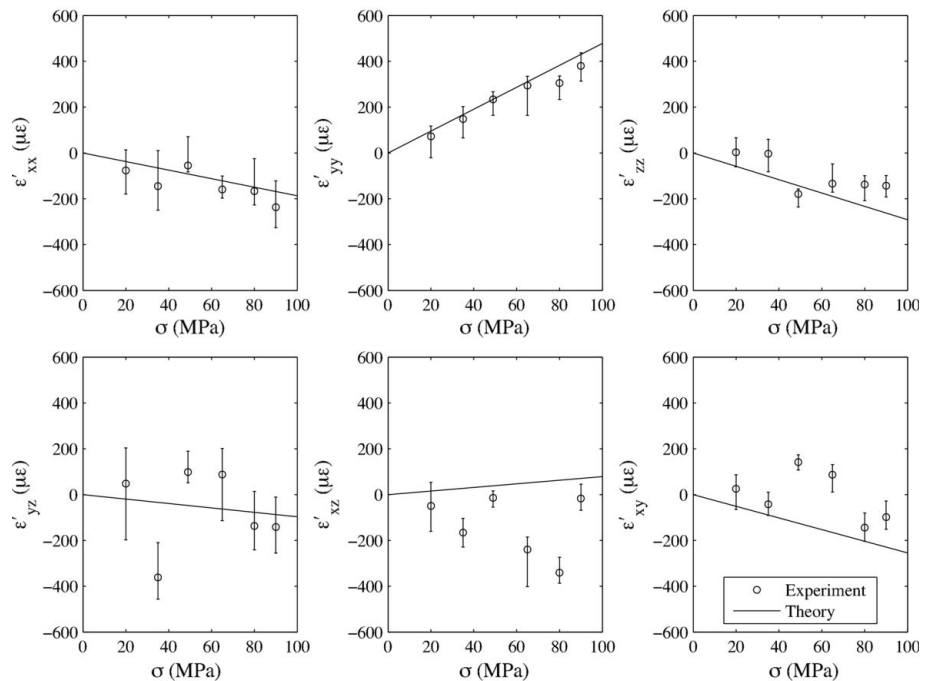

Figure 6
Components of the deviatoric lattice strain tensor are plotted as a function of macroscopic axial load. Error bars represent minimum and maximum values for each area scan. Normal strains agree well with anisotropic elasticity theory, but shear strains do not. The discrepancy in shear components is attributed to measurement noise coupled with limited pole figure coverage.

shown as a solid line. The wire is loaded in the y-direction. Thus, the normal strain in the y-direction is positive. Normal strains in the x- and z-directions exhibit Poisson-like contraction. The relationship between lattice strain and macroscopic load is expected to be linear in the elastic regime. The experimental shear strain components exhibit greater deviation from linearity than the experimental normal strain components, which implies greater error in the shear components. Deviation between average measured strain and theoretical strain is also indicative of measurement error. Normal strain components agree well with theoretical values, whereas shear strain components do not. In addition, the range of strain measured at a fixed load step is greatest for shear components ε'_{yz} and ε'_{xz}. The differences in error magnitude between the normal and shear components is indicative of component-wise differences in measurement uncertainty. The reason for the differences in uncertainty is examined in the subsequent section.

4. Discussion

4.1. Uncertainty analysis

There are two main sources of lattice strain uncertainty in the diffraction experiment. The first source is uncertainty in the diffraction peak positions on the detector plane. Peak position uncertainty is dependent on detector distortion, detector spatial resolution, diffraction geometry, peak fit model and quality of the diffraction peaks. The spatial distortion is corrected within the MAR acquisition software and shown to be insignificant after correction, as tested on a piece of perfect silicon crystal (Kunz *et al.*, 2009). The contribution of detector distortion to peak position uncertainty is, therefore, not considered in this paper. Without analytic peak fitting, peak position uncertainty is of the order of the spatial resolution of the detector (± 1 pixel). Analytic peak fitting reduces the uncertainty in the peak positions by about an order of magnitude. Therefore, an estimate of the peak position uncertainty at a 95% confidence interval for good quality diffraction peaks is ± 0.1 pixel. Peak quality is reduced by plastic straining. The high dislocation density produced by plastic straining causes peak smearing and fragmentation (Ice & Pang, 2009) resulting in larger peak position uncertainty. Plastic straining effects were not an issue in the present experiment because the wire was annealed prior to loading and because the stress remained below the yield point.

The second source of uncertainty is uncertainty in the geometric model used to calculate lattice plane unit normals from the detector peak positions. Uncertainties in the values of the geometric model parameters are quantified using the distributions of measured geometric parameters. The true values of the parameters are assumed to be equal to the mean. For a single load step there are 100 diffraction images. Each image contains about two calibrant patterns on average for a total of about 200 sets of geometric parameters. The uncertainty u in the mean geometric model parameters at a 95% confidence level is calculated assuming a normal distribution,

$$u = \pm 1.96\, S/N^{1/2}, \qquad (8)$$

where S is the standard deviation of the measured detector parameters and N is the number of calibrant patterns (Dunn, 2010). The maximum uncertainty across all six load steps is taken to represent the uncertainty in the geometric model parameters. Uncertainties in the X and Y positions of the detector are ± 0.04 pixels ($\pm 5\ \mu m$) and ± 0.07 pixels ($\pm 9\ \mu m$), respectively. Uncertainty in the sample-to-detector distance is $\pm 4\ \mu m$, and the uncertainty in the detector pitch (X-rotation) and yaw (Z-rotation) are both $\pm 0.005°$. The thickness of the calibrant layer, estimated at 30 μm, contributes to the uncertainty in the Y-position of the detector. For this reason the detector Y-position has greater uncertainty than the X-position. Additional uncertainty in the geometric model is introduced by sample translation during the area scan. There is some variation in geometric model parameters owing to imperfect alignment of the wire and stage translation axes. For a 10 μm × 10 μm area scan the variation in the geometric model parameters owing to stage translation is at least an order of magnitude less than the corresponding uncertainties determined from the calibrant. Thus uncertainties in the geometric model parameters owing to stage translation are negligible for this particular experiment.

Monte Carlo analysis was performed to quantify uncertainty in the deviatoric lattice strain components. A noiseless diffraction pattern was simulated for an unstrained crystal. For 10^5 trials, random perturbations were introduced into either the peak position data, geometric model parameters or both. Perturbations were chosen randomly from a normal distribution with zero mean and 95% confidence interval equal to the uncertainty in the relevant quantity as determined by the experiment. Geometric model parameters were assumed to be uncorrelated. Lattice strain and rotation were then calculated for each trial using the noisy data and parameters. Since, for this analysis, the true value of the lattice strain is zero, the strain error is equal to the calculated strain. Similarly, the rotation error is equal to the calculated rotation. The uncertainty in each strain and rotation component was calculated by evaluating the 95% confidence interval of the resulting error distributions.

The calculated uncertainties are presented in Table 1. Uncertainties in both peak positions and geometric model parameters contribute to the lattice strain uncertainty. Strain uncertainty owing to peak position uncertainty is larger than that owing to geometric model uncertainty. The total uncertainty is different for each strain component. Shear components ε'_{yz} and ε'_{xz} exhibit the greatest uncertainty. The uncertainty in ε'_{yz} is almost four times larger than the uncertainty in ε'_{zz}. The large uncertainties in ε'_{yz} and ε'_{xz} are consistent with the large experimental errors in these components observed in the present study.

Two-dimensional spatial maps of deviatoric lattice strains measured by Chen *et al.* (2011) and Chao *et al.* (2009) also provide evidence of greater uncertainty in shear components ε'_{yz} and ε'_{xz}. These measurements exhibit sharp local gradients that are present only in certain strain components. These

Table 1
Uncertainties of strain and rotation components calculated using Monte Carlo simulations.

Strain uncertainties are in μɛ and rotation uncertainties are in 1/1000°.

	ε'_{xx}	ε'_{yy}	ε'_{zz}	ε'_{yz}	ε'_{xz}	ε'_{xy}	α	β	γ
Peak position	±70	±64	±45	±221	±147	±70	±11.9	±7.4	±4.4
Geometric model	±46	±24	±39	±75	±46	±31	±2.0	±0.7	±5.8
Combined	±84	±68	±59	±233	±154	±77	±12.0	±7.4	±7.3

sharp local gradients are likely artifacts of measurement noise and are therefore indicative of greater measurement uncertainty. Deviatoric lattice strain maps of plastically deformed quartz (Chen *et al.*, 2011) exhibit sharp local gradients in ε'_{yz} and ε'_{xz}, suggesting greater uncertainty in these components. Similarly, deviatoric lattice strain maps of plastically deformed nickel-base Alloy 600 (Chao *et al.*, 2009) exhibit sharp local gradients in ε'_{xz}. These works support the conclusion that measurement uncertainty is different for each lattice strain component, with shear components ε'_{yz} and ε'_{xz} having the greatest uncertainties.

4.2. Spurious deformation modes

The large uncertainties in ε'_{yz} and ε'_{xz} can be explained by the existence of spurious deformation modes. Spurious deformation modes are deformations that tend to arise erroneously in the deformation gradient calculation owing to measurement noise and limited pole figure coverage. The spurious deformation modes can be identified by examining the correlations between strain and rotation errors computed

Table 2
Correlation coefficients between strain and rotation errors calculated using Monte Carlo simulation.

A value of ±1 indicates perfect correlation, whereas a value of 0 represents no correlation.

	ε_{xx}	ε_{yy}	ε_{zz}	ε_{yz}	ε_{xz}	ε_{xy}	α	β
ε_{yy}	−0.71							
ε_{zz}	−0.59	−0.14						
ε_{yz}	0.21	0.06	−0.36					
ε_{xz}	−0.04	0.08	−0.04	0.12				
ε_{xy}	0.05	−0.01	−0.05	0.04	−0.22			
α	0.29	0.04	−0.45	0.97	0.13	0.05		
β	0.03	−0.08	0.05	−0.14	−0.94	0.13	−0.15	
γ	−0.03	0.03	0.01	0.00	0.34	−0.64	0.00	−0.17

from the Monte Carlo simulation. The simulation with uncertainties in both peak positions and geometric model parameters is considered. Scatter plots of strain and rotation errors are presented in Fig. 7. The data form ellipsoids. For quantities that are not correlated, the principal axes of the ellipse lie along the coordinate axes. The principal axes are rotated away from the coordinate axes as the level of correlation increases. Correlation coefficients are presented in Table 2. There is a strong 97% correlation between ε'_{yz} and α, which points to the existence of a coupled yz-shear and x-rotation mode. There is also a strong 94% negative correlation between ε'_{xz} and β which suggests a coupled xz-shear and y-rotation mode. A 71% negative correlation between ε'_{xx} and ε'_{yy} uncovers an xy-extension/contraction mode. The xy-extension/contraction mode is an isochoric deformation in the xy-plane. One might therefore expect xy-shear, which is also an isochoric deformation in the xy-plane, to be a spurious deformation mode.

Pole figures depicting the angular changes in lattice plane normal directions for the four spurious deformation modes are plotted in Fig. 8 using an equal area projection. The angle changes correspond to an effective strain of 100 μɛ. The region from which lattice plane normals are sampled by the experiment is outlined in white. Lattice plane normals within the sampling
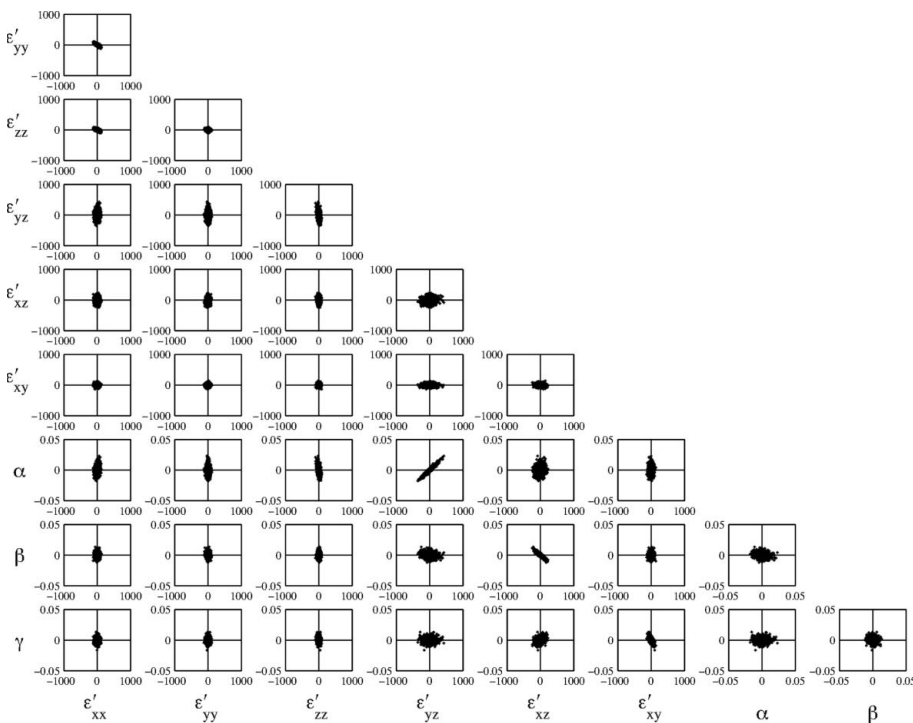

Figure 7
Scatter plots of strain and rotation errors calculated using Monte Carlo simulation of the diffraction experiment. Strains are expressed in microstrain and rotations are expressed in degrees. There is a high correlation between yz-shear and rotation about the x-axis (α) and between xz-shear and rotation about the y-axis (β).

(a) yz-shear and x-rotation   (b) xz-shear and y-rotation

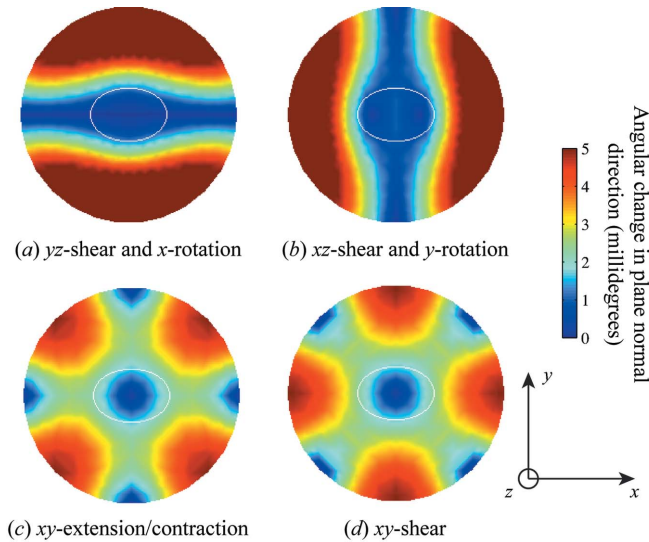(c) xy-extension/contraction   (d) xy-shear

Figure 8
Pole figures depicting the angular change in lattice plane normal direction for four spurious deformation modes at an effective strain of 100 µε. The sampling region is enclosed by a white outline. The movements of the sampled lattice plane normals are relatively insensitive to these deformation modes. As a result, these deformation modes can spuriously arise in the deformation gradient calculation owing to measurement noise.

region are closely aligned with the sample z-axis. Spurious deformation modes produce relatively small changes to lattice plane normal directions in the sampling region. Considering only the sampling region, spurious deformation modes appear similar to an identical mapping that does not produce any deformation. In the presence of measurement noise, it can be difficult to discern between a spurious deformation mode and an identical mapping. As a result, spurious deformation modes can arise in the deformation gradient calculation, which in turn gives rise to strain and rotation errors. Spurious deformation modes contribute to the uncertainty of the strain and rotation components associated with each mode.

The angle change in the sampling region is a measure of the signal-to-noise ratio for a given deformation mode. Signal is lowest for the coupled shear-rotation deformation modes. Consequently, ε'_{yz} and ε'_{xz} exhibit the greatest experimental error. Signal amplitude is slightly higher for xy-extension/compression and xy-shear deformation modes, which accounts for the errors in ε'_{xy}.

The precision of the lattice strain measurements would be increased by increasing pole figure coverage. This could be accomplished by using a larger area detector or multiple detectors. Lattice strain measurements could also be improved by using a detector with higher spatial resolution to reduce measurement noise.

5. Conclusions

Polychromatic X-ray microdiffraction was used to measure deviatoric lattice strain in a wire specimen loaded *in situ* under uniaxial tension. The local strain state at the measurement site

was determined from anisotropic elasticity theory. The measured normal strain components agree well with theory, but the shear strain components do not. Uncertainties in the diffraction peak positions and geometric model parameters propagate to the lattice strain uncertainty. Uncertainty analyses conducted using Monte Carlo simulations of the diffraction experiment show that shear components ε'_{yz} and ε'_{xz} have greater uncertainty than the normal strain components. The large uncertainties in the shear strains are due to measurement noise and limited pole figure coverage. Lattice strain measurement could be improved by using a larger detector or multiple detectors to increase pole figure coverage. Precision could also be improved by increasing detector spatial resolution.

APPENDIX A
Lattice plane unit normal mapping

The local deformation F is multiplicatively decomposed into a lattice-uncoupled deformation F^p followed by a lattice-coupled deformation F^* as outlined in equation (2) and illustrated schematically in Fig. 5. The subscript 0 denotes values in the reference configuration, and an overbar denotes values in the intermediate configuration. Values in the deformed configuration are unadorned.

Consider the lattice-coupled deformation from the intermediate configuration to the deformed configuration. For lattice-coupled deformation, lattice vectors transform in the same manner as material vectors. Two differential lattice vectors $\bar{\mathbf{a}}$ and $\bar{\mathbf{b}}$ define a lattice plane in the intermediate configuration (Fig. 9). The lattice vectors map according to

$$\mathbf{a} = F^*\bar{\mathbf{a}}, \qquad \mathbf{b} = F^*\bar{\mathbf{b}}. \qquad (9)$$

The lattice plane normals are calculated from the cross product of the lattice vectors,

$$\bar{\mathbf{n}} = \bar{\mathbf{a}} \times \bar{\mathbf{b}}, \qquad \mathbf{n} = \mathbf{a} \times \mathbf{b}. \qquad (10)$$

The magnitude of a lattice plane normal is the differential area of the parallelogram defined by the two lattice vectors

$$\bar{\mathbf{n}} = \bar{A}\hat{\bar{\mathbf{n}}}, \qquad \mathbf{n} = A\hat{\mathbf{n}}, \qquad (11)$$

where $\bar{A}$ and A are differential areas and $(\hat{\cdot})$ denotes a vector of unit length. Combining (9)–(11) and applying a vector identity yields Nanson's formula (Reddy, 2008),

$$A\hat{\mathbf{n}} = J^* F^{*-\mathrm{T}} \bar{A}\hat{\bar{\mathbf{n}}}, \qquad (12)$$
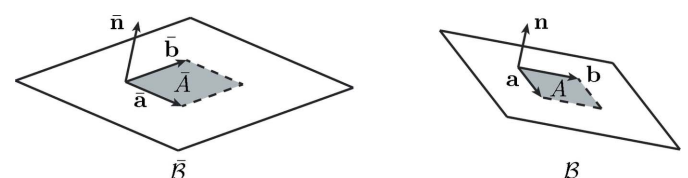
where $J^* = \det F^*$. Rearranging terms yields

Figure 9
A lattice plane in the intermediate and deformed configurations.

$$F^{*\mathrm{T}} \hat{\mathbf{n}} = c\hat{\bar{\mathbf{n}}}, \qquad (13)$$

$$c = J^* \bar{A}/A, \qquad (14)$$

where c is a scale factor. Since the lattice-uncoupled deformation does not change lattice structure or orientation, lattice plane unit normals are the same in both the reference and intermediate configurations $\hat{\mathbf{n}}_0 = \hat{\bar{\mathbf{n}}}$. The mapping of lattice plane unit normals from the initial configuration to the deformed configuration is therefore described by

$$F^{*\mathrm{T}} \hat{\mathbf{n}} = c\hat{\mathbf{n}}_0. \qquad (15)$$

References

Chao, J., Mark, A., Fuller, M. L. S., McIntyre, N. S., Holt, R. A., Klassen, R. J. & Liu, W. (2009). *Mater. Sci. Eng. A*, **524**, 20–27.

Chen, K., Kunz, M., Tamura, N. & Wenk, H.-R., Chen, K., Kunz, M., Tamura, N. & Wenk, H.-R. (2011). *Eur. J. Mineral.* **23**, 169–178.

Chung, J. & Ice, G. (1999). *J. Appl. Phys.* **86**, 5249–5255.

Dunn, P. F. (2010). *Measurement and Data Analysis for Engineers.* Boca Raton: CRC Press.

Edmiston, J. K., Barton, N. R., Bernier, J. V., Johnson, G. C. & Steigmann, D. J. (2011). *J. Appl. Cryst.* **44**, 299–312.

Frank, F. C. (1988). *Eighth Internation Conference on Textures of Materials*, edited by J. S. Kallend and G. Gottstein, pp. 3–13. Warrendale: The Metallurgical Society.

Ice, G. E. & Pang, J. W. L. (2009). *Mater. Charact.* **60**, 1191–1201.

Kunz, M., Tamura, N., Chen, K., MacDowell, A. A., Celestre, R. S., Church, M. M., Fakra, S., Domning, E. E., Glossinger, J. M., Kirschman, J. L., Morrison, G. Y., Plate, D. W., Smith, B. V., Warwick, T., Yashchuk, V. V., Padmore, H. A. & Ustundag, E. (2009). *Rev. Sci. Instrum.* **80**, 035108.

Larson, B., Yang, W., Ice, G., Budai, J. & Tischler, J. (2002). *Nature (London)*, **415**, 887–890.

Ledbetter, H. (2001). *Handbook of Elastic Properties of Solids, Liquids and Gases*, Vol. 3, edited by M. Levy, ch. 17, pp. 291–297. New York: Academic Press.

Marin, E. & Dawson, P. (1998). *Comput. Methods Appl. Mech. Eng.* **165**, 1–21.

Reddy, J. N. (2008). *An Introduction to Continuum Mechanics.* Cambridge University Press.

Tamura, N., MacDowell, A. A., Spolenak, R., Valek, B. C., Bravman, J. C., Brown, W. L., Celestre, R. S., Padmore, H. A., Batterman, B. W. & Patel, J. R. (2003). *J. Synchrotron Rad.* **10**, 137–143.

Tamura, N., Padmore, H. & Patel, J. (2005). *Mater. Sci. Eng. A*, **399**, 92–98.

Zhang, H. (2009). PhD thesis, Lehigh University, USA.